



Experimental and Numerical Investigations of Magnetohydrodynamic Hypersonic Interactions for High-Altitude Flight

Benjamin Khiar¹, Viviana Lago², Federico Boni³

Abstract

We present preliminary experimental and numerical results on the interaction between hypersonic ionized plasma flows and magnetized coin-shaped models. In the experiments, a magnetic field is generated by placing cuboid neodymium magnets directly behind models fabricated from various metallic materials. High-speed CMOS camera observations of the plasma-model interaction reveal substantial alterations in plasma self-emission in the presence of the magnetic field, with a pronounced dependence on magnet orientation. These modifications are attributed to high levels of electron magnetization, characterized by Hall parameter values reaching several dozen. Further analysis provides insights into the magnetic field's effects on shock standoff distance and model surface condition. Direct Simulation Monte Carlo (DSMC) numerical simulations are employed to characterize the flow, particularly MHD-relevant quantities such as the full tensorial electrical conductivity. Additionally, a simple "test-particle" solver is used to evaluate charged particle trajectories under the influence of the magnetic field and collisions. These findings offer initial insights into the mechanisms underlying the experimentally observed changes in emission patterns.

Keywords: magnetohydrodynamics, hypersonics, re-entry, MHD

Nomenclature

I atin

B - magnetic field [T]

E – Electric field [V/m]

j – Electric current [A/m²]

v – Flow velocity [m/s]

T - Temperature [K]

n – Density [m $^{-3}$]

 σ – Electric conductivity [S/m]

 Ω_e – Hall parameter

 $e \, - \, \operatorname{Elementary\ charge\ [C]}$

m - Particle mass [kg]

1. Context

Shortly after the dawn of the space age, early studies proposed manipulating ionized flows during atmospheric reentry using magnetic fields [1, 2]. Potential applications were quickly identified, including deceleration and control of reentry vehicles, reduction of heat flux to vehicle surfaces, and mitigation of frictional forces. However, significant technological challenges were noted, such as the complexity of the underlying physics, achieving sufficient electrical conductivity in the flow, developing relevant magnetic field generation systems, and addressing issues related to interactions between ionized flows and wall-mounted electrodes. In the United States, initial experimental validation of MHD's potential was demonstrated by observing an increased shock standoff distance in the presence of a magnetic field [3]. This parameter, central to subsequent magnetohydrodynamics (MHD) studies, is relatively easy to measure and enables direct comparison with theoretical and numerical models [4].

¹Physics Instrumentation and Space Department, ONERA, Université Paris-Saclay, 91123 Palaiseau, France, benjamin.khiar@onera.fr

²Laboratoire ICARE, CNRS, 1 C Av de la Recherche Scientifique, Orléans, France, viviana.lago@cnrs-orleans.fr

³Physics Instrumentation and Space Department, ONERA, Université Paris-Saclay, 91123 Palaiseau, France, federico.boni@onera.fr

Concurrently, a vibrant research field emerged around MHD electrical generators, aiming to develop high-power (up to 32 MW), efficient (70 % efficiency), and reliable (no moving parts) systems [5]. Challenges, including material constraints (operation at high temperatures of 2000–3000 K), physical instabilities (e.g., Velikhov instability in bi-temperature operation [6]), and limitations in early superconducting magnet technology, hindered widespread adoption. Nevertheless, these efforts provided valuable insights into the physics relevant to reentry MHD, particularly regarding flow electrical conductivity. Mastering this parameter is critical for achieving strong magnetic field-flow interactions. This interaction is quantified by the dimensionless MHD interaction parameter Q, defined as ($Q = \frac{\sigma B^2 L}{\sigma R}$), where σ is the electrical conductivity of the flow, B is the magnetic field strength, L is the characteristic length of the MHD interaction zone, ρ is the flow mass density, and v is its velocity [7]. The parameter O measures the relative strength of MHD forces compared to hydrodynamic inertial forces. A higher O indicates greater magnetic influence on the flow, achievable by increasing conductivity, magnetic field strength, or interaction zone size. MHD effects are more pronounced at low densities (high altitudes) and lower velocities. However, during reentry, conductivity depends heavily on flow velocity due to high post-shock temperatures. Insufficient velocity may prevent natural ionization via shock heating, rendering MHD ineffective unless alternative ionization methods are employed.

To address conductivity challenges, techniques such as seeding the flow with easily ionizable alkali metals were extensively studied for MHD generators [5]. Advances in magnetic confinement fusion research have also driven progress in high-field magnet technologies, such as high-temperature superconductors, benefiting reentry MHD applications [8]. In parallel, computational advancements have enabled diverse teams to explore MHD actuator concepts for various applications, including Earth reentry for blunt bodies like OREX [9], RAMC [10], Martian reentry vehicles like Mars Pathfinder [11], aerobraking/capture strategies for solar system exploration [12], and mitigation of radio blackout phenomena [13]. These studies typically couple computational fluid dynamics with MHD-specific modeling to resolve electromagnetic fields, currents, and associated forces. Notable contributions have come from Japanese research groups, including those led by Professors Otsu (Ryukoku University) and Fujino (Tsukuba University).

A persistent need across these efforts is for comprehensive, precise experimental data covering a wide range of flight regimes. Existing experimental studies, conducted in facilities like shock tubes [14, 15] or plasma torch wind tunnels [16], often provide limited data, insufficient for a complete understanding of hypersonic MHD interactions or the full potential of MHD actuators during a typical reentry trajectory. Noteworthy experimental work includes that of Professor David Gildfind's team at the University of Queensland using the X2 facility [17, 14, 18].

2. The AMHYRA project

The 3-year long AMHYRA project aims to advance scientific and technical understanding of hypersonic flow manipulation using electromagnetic forces, with a focus on magnetohydrodynamic (MHD) physics. The AMHYRA project brings together the expertise, facilities, and modeling tools of ONERA and CNRS, through the ICARE Institute, to master the complex physics of MHD interactions in hypersonic regimes. A key objective is to create an experimental database encompassing a wide range of flight conditions, simulating those encountered during atmospheric reentry. This database, including data on shock wave distances, shapes, and aerodynamic forces, will be generated using models equipped with magnetic field generation devices. Experiments will be conducted across three facilities: MARHy, PHEDRA (CNRS/ICARE) [19], and F4 (ONERA) [20]. Each facility will enable the study of distinct aspects of hypersonic MHD, such as discharge-magnetic field interactions (MARHy), the influence of MHD on material ablation (PHEDRA), and MHD with "real gas" effects (F4).

In parallel, significant numerical modeling efforts will be undertaken using ONERA's MHD and plasma simulation tools (TARANIS [21] RHEI [22]...). This synergy between experimental and numerical approaches will facilitate critical validation and comparison, paving the way for the maturation of more advanced MHD actuator concepts, particularly for improving the maneuverability of hypersonic vehicles.

2.1. PHEDRA: An Experimental Facility Tailored for MHD Studies

The PHEDRA wind tunnel generates supersonic/hypersonic, low-pressure ionized flows to study the properties of high-enthalpy flows surrounding hypersonic vehicles during atmospheric reentry. Measuring 4.3 meters in length and 1.1 meters in diameter, PHEDRA is equipped with an arc-jet generator. Continuous operation is maintained by a three-stage pumping system, which sustains a residual pressure of approximately 2–8 Pa in the vacuum chamber during experiments. The flow is produced by a generator comprising a conical nozzle and a cathode. The gas passing through the nozzle throat is ionized by an electric arc sustained by the cathode, powered by a current-regulated electrical source. Electrical parameters vary with currents ranging from 50 to 250 A and mass flow rates from 0.1 to 0.5 q/s, achieving specific enthalpies of 5 to 50 MJ/kg.

Key advantages of this plasma generator include the stability of plasma jets over several hours, the large flow dimensions (500 mm in diameter and 1500 mm in length at 0.1 Torr), and minimal plasma contamination due to cathode erosion rates below 1 ng/s relative to a minimum mass flow rate of 0.1 g/s. The PHEDRA facility is equipped with specialized instrumentation to monitor plasma operating parameters and measure specific enthalpy in real time. A variety of gases can be used, including argon, nitrogen, air, and mixtures containing CO_2 to simulate the Martian atmosphere or CH_4 for Titan's atmosphere.

Additionally, tailored diagnostic tools have been developed for the specific conditions of PHEDRA to analyze flow characteristics. For a comprehensive overview of the PHEDRA wind tunnel, refer to [23].

3. Preliminary MHD experimental results on PHEDRA

3.1. Experimental setup with coin-shaped models

A schematic of the experimental configuration is presented in Fig 1(a). The model is positioned along the central axis of the arc-jet plasma generator, at a variable distance of 3 to 10 cm from the nozzle exit.

Flow visualization is conducted using an CMOS Kuro camera to examine the interaction between the model and the plasma under various experimental conditions. A thermal camera (OPTRIS 640) is mounted above the plasma source to monitor and evaluate the surface temperature of the model. Additional diagnostics can be incorporated as needed to further characterize the plasma-model interaction. These include spectrometers to analyze the plasma flow composition/temperature and probes - such as Langmuir probes and microwave resonant curling probes [24] - to measure electron density across the shock layer and in the free stream. Curling probes are a recent development in this context [25]; they are compact and can be flush-mounted into the model walls. Unlike Langmuir probes, which can be intrusive due to current collection, curling probes are low intrusive, relying instead on measuring the resonance frequency shift, which depends on the relative permittivity of plasma and is directly linked to the electron density.

This study employs a coin-shaped disk model with dimensions of 35 mm in diameter and 3 mm in thickness (see Fig 1(b)). The model is constructed from five distinct materials—tungsten, titanium, niobium, molybdenum, and tantalum—selected for their relevance to high-temperature hypersonic/re-entry applications. The coin-like geometry is chosen for its straightforward integration near the stagnation point and its compatibility with simplified numerical simulations.

The disk is affixed to a 38 mm diameter, 50 mm long alumina support cylinder using Resbond 905 ceramic adhesive (see Fig 1(b)). The assembly is mounted on a mechanical piston system, enabling precise positioning of the model within or outside the plasma jet. The setup accommodates two models simultaneously: while one is immersed in the plasma jet, the other remains fully retracted, and vice versa. A third configuration allows both models to be positioned outside the plasma jet (see Fig 1(c)).

The magnetic field in the experiments is generated by two neodymium magnets, each measuring $20 \times 20 \times 10$ mm, bonded with their north and south faces aligned to form a single magnetic unit. The neodymium magnets are positioned within the alumina support cylinder directly behind the coin-shaped model, as illustrated in Fig 2(a). The magnetic field distribution is simulated using the Finite Element

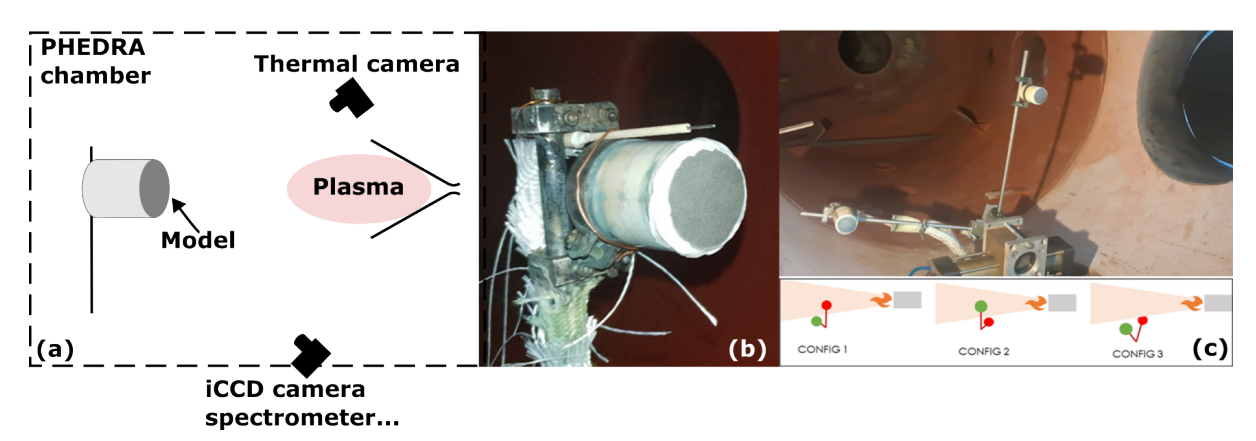


Fig 1. (a) Schematic view of the experimental setup in the PHEDRA chamber (b) photograph of a mounted coin-shaped model (c) Two-arms mechanical mounting system

Method Magnetics (FEMM) software [26], with results depicted in Fig 2(b). The peak magnetic field near the magnet surface reaches approximately 0.7 T, while at a distance of 5 mm, close to the model surface, the field strength is approximately 0.4 T.

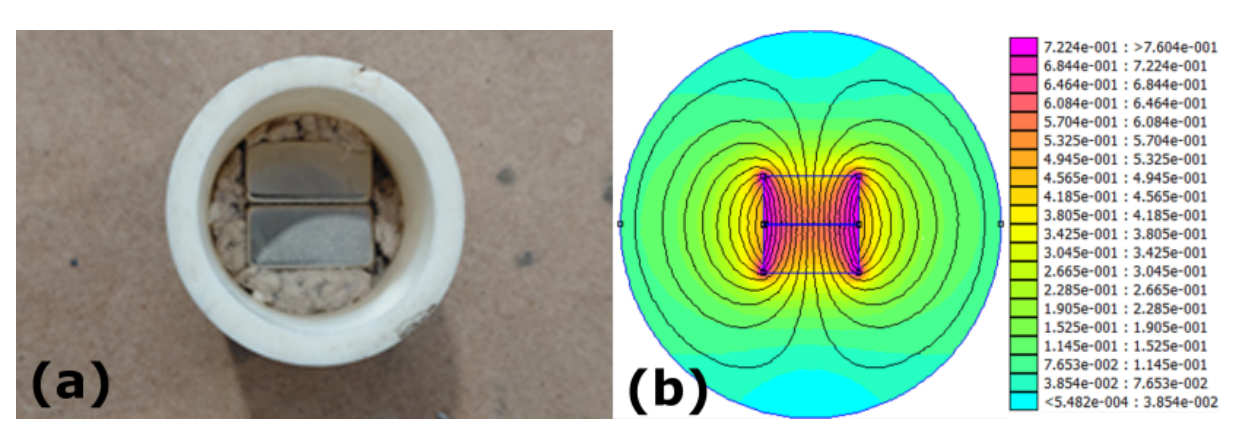


Fig 2. (a) Rear view of two neodymium magnets inserted behind the model (b) Magnetic field from the magnets as obtained from FEMM software

3.2. Experimental observed effects induced by the magnetic field

3.2.1. Influence of magnetic field orientation

A qualitative study was conducted to assess the impact of magnets placed behind the model by analyzing self-emission images of the plasma, captured using the CMOS camera. The results were obtained in an air plasma with an arc current of 150 A and an air mass flow rate of 0.32 g/s, corresponding to a discharge power ranging between 8.4 and 8.7 kW, the pressure in the experimental chamber ranges between 6 and 6.2 Pa. The model was positioned 5 cm downstream of the nozzle exit. Fig 3 presents the steady-state plasma self-emission for four distinct configurations: (a) no magnet present, (b) magnet magnetization aligned with the flow direction, (c) magnet magnetization perpendicular to both the flow direction and the camera's line of sight, and (d) magnet magnetization perpendicular to the flow direction but aligned with the camera's line of sight.

Configuration (a) clearly shows a bow shock with a large stand-off distance, resulting from the low-pressure experimental conditions. A brighter region appears near the model surface, corresponding to the reactive boundary layer. In configuration (b), the natural shape shock is modified as a prominent triangular-shaped region of intense emission forms at the center of the model surface, corresponding to the area where magnetic field lines converge toward the magnet's pole. In contrast, configuration (c)

exhibits a reduction in self-emission at the central region compared to the no-magnetic-field case (a). Notably, arch-like structures appear near both extremities of the model, suggesting that components of the flow may be aligning with the magnetic field lines. In configuration (d), the overall emission pattern closely resembles that of case (a), with a slight asymmetry characterized by enhanced emission in the lower region. Configurations (c) and (d) are fundamentally identical, as both the incoming flow and the model are axisymmetric, differing only in the camera's perspective. This indicates that, unlike configuration (b), these setups disrupt the axisymmetric nature of the plasma-model interaction which could lead to aerodynamic vectorization.

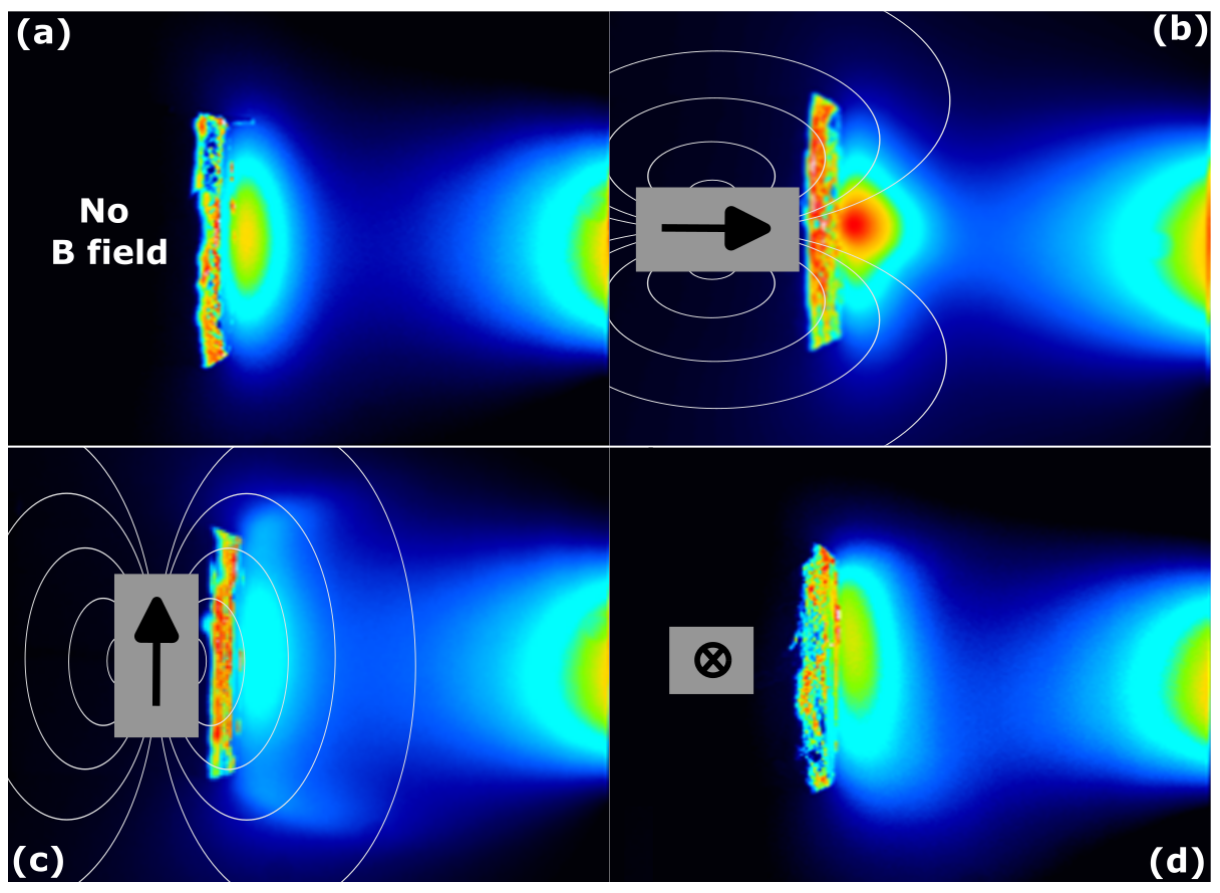


Fig 3. Self-emission from the following setups: (a) No magnets (b) Magnet magnetization aligned with the flow (c) magnet magnetization perpendicular to both the flow direction and the camera's line of sight and (d) magnet magnetization perpendicular to the flow direction but aligned with the camera's line of sight

3.2.2. Quantitative changes in plasma self-emission

To quantitatively assess the magnetic field's impact on plasma self-emission, as qualitatively described in the previous section, Fig. 4 presents maps illustrating the differences in plasma self-emission between the no-magnetic-field and magnetized cases, expressed as emissivity ratios. These maps were generated by normalizing the intensities relative to the emission at the nozzle exit under freestream conditions. Careful measures were implemented to maintain consistent observational times across experiments, facilitating reliable comparisons of absolute plasma emission values under varying test conditions.

As evident in Fig. 4, the magnetic field induces substantial variations in plasma self-emission. The previously noted "arches" correspond to emission increases exceeding 100%, while the central region exhibits a decrease of more than 70%. Assuming a direct correlation between self-emission and electron density distribution, these observations suggest the presence of electron "depletion" and "enrichment"

2.2 2.0 1.8 1.6 1.4 1.2 0.9 0.7 0.5 0.3

regions, following a pattern that aligns with the magnetic B-field distribution.

Fig 4. Resulting image obtained from the ratio of image b) and a)

3.2.3. Influence of material properties on shock standoff distance and model surface state

To assess the influence of the magnetic field on various model materials, a methodology was developed to derive reliable shock standoff distance measurements across different cases. The results, presented in Table 1 for five materials—tungsten, titanium, niobium, molybdenum, and tantalum—correspond to the configuration shown in Fig 2(c), where the magnet magnetization is oriented perpendicular to the main flow direction.

The results demonstrate that the shock standoff distance increases in the presence of a magnetic field across all tested materials, although the degree of this increase varies by material. The most significant enhancements are observed with tungsten and niobium models, showing increases of approximately 17% and 16%, respectively. Increases in shock standoff distance are a common finding in published experimental studies; however, as will be explored later, the MHD interactions in those investigations typically occur under substantially different regimes.

Additional insights into the magnetic field effects are provided in Fig. 5, which shows photographs of the model surfaces after exposure to the plasma flow, both without a magnetic field (top row) and with a magnetic field (bottom row). Efforts were made to ensure equivalent exposure times of 6 mn for each paired comparison. The primary observation is that the magnetic field influences the resulting surface condition of the models, with variations in the extent of this effect depending on the material. These findings suggest that the magnetic field alters the parameters governing material degradation such as

Table 1. Shock standoff distance increase relative to the no B-field case. Magnet magnetization along the flow direction.

Model material	Standoff increase %
Tungsten	+17.24
Titanium	+8.48
Niobium	+15.61
Molybdenum	+2.75
Tantalum	+2.62

oxydation, potentially through modifications to thermal fluxes, plasma composition, surface chemistry, or, more likely, a combination of these processes. The most prominent case is that of niobium, which exhibits the formation of a substantial oxide layer when no magnetic field is applied.[27]

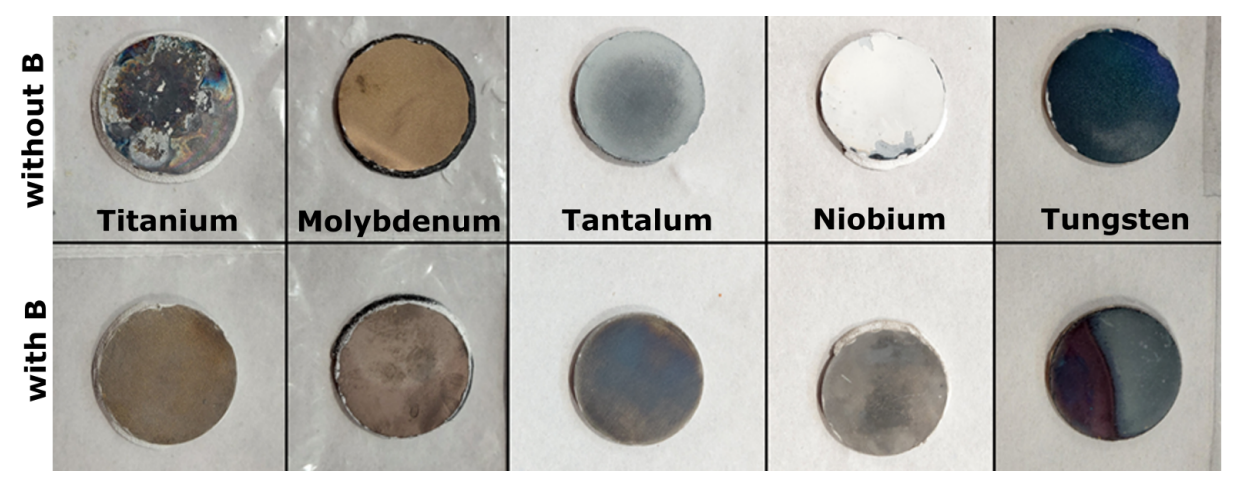


Fig 5. Model surfaces after 6 mn exposure to the air plasma flow: (top row) without B-field (bottom row) with magnetic field

4. DSMC investigation of the PHEDRA argon plasma

To better characterize a PHEDRA-type interacting plasma flow over the model, particularly in the presence of a magnetic field, two-dimensional axisymmetric (r-z) DSMC simulations were performed using the SPARTA code [28]. These simulations model the interaction between a high-temperature, highvelocity argon plasma and the previously described coin-shaped body. A simplified three-species plasma composition (Ar, Ar⁺, and e⁻) is employed, utilizing a Variable Soft Sphere (VSS) "collision-averaged" model with parameters sourced from [29]. A limitation of the VSS model is acknowledged: its "collisionaveraged" approach may exhibit reduced accuracy at high ionization degrees. A "collision-specific" model would be preferable [30], but its implementation in SPARTA exceeds the scope of this study. The freestream flow temperature is fixed at 2500 K, with a mean bulk velocity of 3500 m/s along the z-axis. Simulations were conducted across a range of total particle number densities from $1.3 \times 10^{20} \, m^{-3}$ to $6.5 \times 10^{20} \, m^{-3}$ and electron fractions from 0.3 % to 2.3 %, yielding freestream electron densities between $10^{18} \, m^{-3}$ and $3 \times 10^{18} \, m^{-3}$. The simulations incorporate SPARTA's ambipolar approximation to bypass the prohibitively short timescales associated with electron dynamics. The ratio of physical to simulated particles is chosen to maintain at least approximately 30 ambipolar Ar⁺ ions per cell. Given the relatively low electron fractions, each cell contains much more than 100 neutral argon particles. Wall interactions are modeled using a simple diffusive reflection scheme, assuming a fixed surface temperature of 1000 K and an accommodation coefficient of 1. Ambipolar Ar⁺ ions are presumed to fully recombine upon surface impact, releasing approximately 15.76 eV (corresponding to argon's first ionization energy). A simplified two-reaction model (electron impact ionization and three-body recombination [31]) was tested but found to have negligible influence under the investigated conditions. The simulation domain comprises a 50.75 \times 72.5 mm (r-z) box, discretized into 210 \times 300 cells for a uniform spatial resolution of $\Delta x \approx 242~\mu m$. Within the modeled freestream density range at 2500 K, the Ar-Ar mean free path (mfp) varies from approximately 2 to 20 mm, resulting in a freestream $\Delta x/mfp$ ratio of \leq 0.12. The time step is set to $\Delta t = 10$ ns. For the highest density case, the neutral collision time is $\tau_{coll} \approx 1.6~\mu s$, yielding a freestream $\delta t/\tau_{coll}$ ratio of approximately 6×10^{-3} . The CFL-like condition is satisfied, with V · Δt / $\Delta x \approx 0.14$.

4.1. Flow characterization

This section provides a concise overview of the primary fields pertinent to our study. In Fig. 6, we present steady-state results for a case with a freestream total density of $1.3 \times 10^{20} \, \text{m}^{-3}$ and an electron density of $3 \times 10^{18} \,\mathrm{m}^{-3}$, corresponding to an ionization degree of \sim 2.3 %. In Fig. 6(a), the neutral density field is shown. The flow compression exhibits characteristics typical of rarefied shocks, featuring a smooth transition from freestream to stagnation density. A maximum density of $\sim 3 \times 10^{21}\,\mathrm{m}^{-3}$ is reached near the model surface, representing a compression factor of \sim 23 for the incoming flow. In Fig. 6(c), the electron density field is displayed. A notably lower density increase between the free stream and the value close to the model wall is observed across the shock transition, with a compression factor of only \sim 2.8 (maximum density of \sim 8.5 \times $10^{18}\,\mathrm{m}^{-3}$). Unlike the neutral density peak, the electron density maximum is located \sim 2.5 mm away from the model surface. These results are consistent with recent experiments using the same model configuration in an argon plasma [25]. Electron density measurements performed with Langmuir and curling probes show values of $\simeq 10^{20}~{\rm m}^{-3}$ across the shock layer and $\simeq 4 \times 10^{19} \text{ m}^{-3}$ in the free stream, corresponding to compression factors of approximately 2.5. Lineouts along the model stagnation line, as illustrated in Fig. 7, reveal that this distribution arises from surface recombination effects. Indeed, comparing the full black line (no wall recombination) with the other three cases clearly demonstrates the dramatic impact of surface recombination on the density profile. An additional insight from the results presented in Fig. 7 is that both the peak electron density and the overall profile shape are influenced by the freestream total density (as evidenced by the dash-dotted and dotted black curves, which differ solely in freestream total density). This dependency could prove valuable for future studies, enabling direct comparisons between experimental self-emission profiles and simulated profiles to achieve more precise flow characterization.

The flow velocity fields is shown Fig. 6(b) where it can be seen that the incoming flow decelerates smoothly at a rate $\sim 0.9~km\cdot s^{-1}\cdot cm^{-1}$. The resulting temperature increase is shown in Fig. 6(d) where a peak temperature at ~ 10000 K is observed at ~ 14 mm away from the model surface, much farther than the peak density location. The temperature profile is strongly influenced by the 1000 K surface temperature set within the diffusive model, as described previously.

We emphasize that the presented results feature a single temperature, whereas these types of experiments typically exhibit at least two distinct temperature populations: one for heavy particles and another for light electrons [32]. In particular, we estimate the thermal equilibration time between the ion and electron populations to be on the order of $\sim\!\!40~\mu\mathrm{s}$ under representative conditions of $T_{\rm heavy}=10000~\mathrm{K}$ and $n_e=5\times10^{18}~\mathrm{m}^{-3}$. For a typical flow velocity of $\sim\!\!1~\mathrm{km/s}$, this corresponds to an equilibration distance of $\sim\!\!4~\mathrm{cm}$. Consequently, non-equilibrium populations are anticipated under these conditions. The ambipolar approximation employed in this modeling work precludes tracking such disequilibria, suggesting that the reported temperature likely overestimates the actual electron temperature.

The quantities briefly outlined in this section are essential for assessing MHD-relevant parameters, as will be demonstrated in the following section. Although some uncertainties persist in the flow parameters, we can assert with reasonable confidence that these quantities offer a robust insight into the MHD-relevant parameters governing the PHEDRA experiments.

4.2. MHD-relevant flow parameters

An essential quantity for estimating MHD parameters is the electron collision frequency. Fig. 8(a) presents a map of the steady-state total electron collision frequency for the case described in the previous section. This frequency is calculated as the sum of the electron-ion and electron-neutral collision fre-

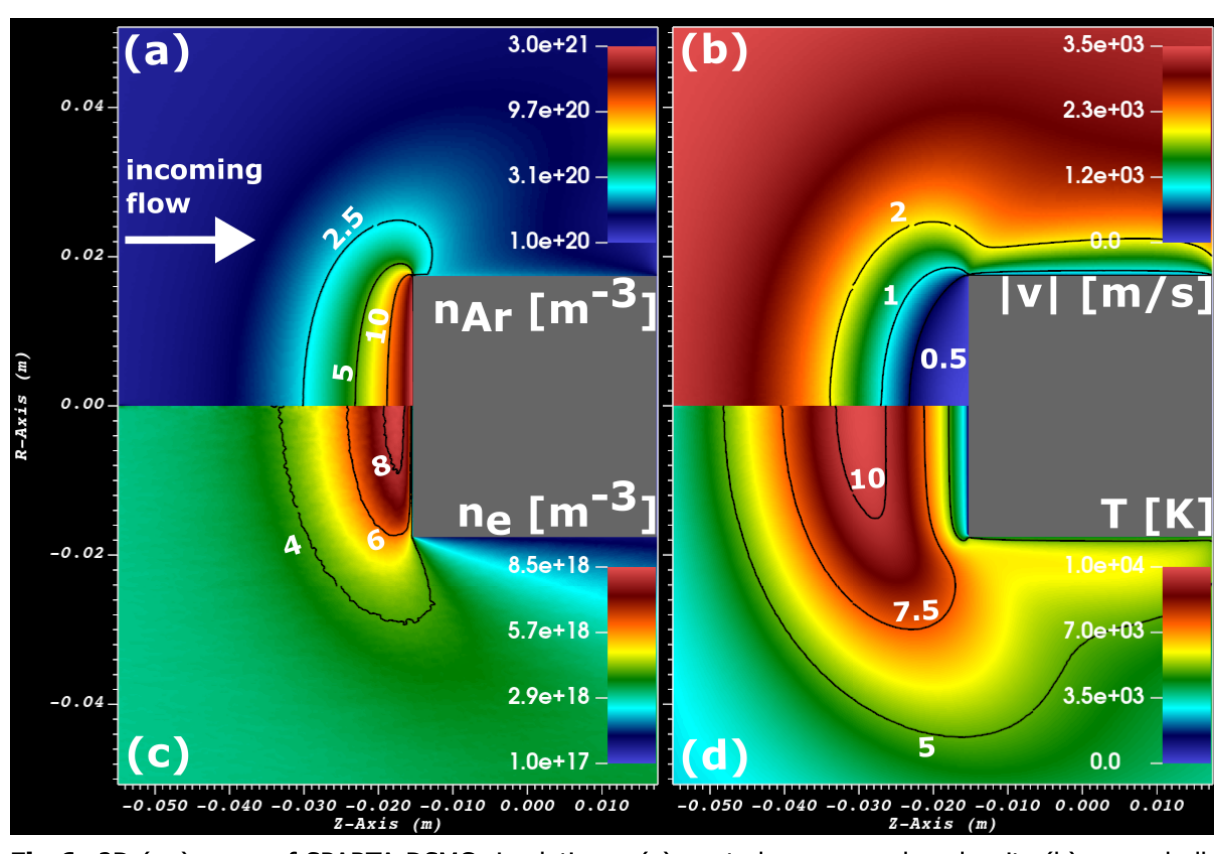


Fig 6. 2D (r-z) maps of SPARTA DSMC simulations: (a) neutral argon number density (b) argon bulk velocity lagnitude (c) electron number density and (d) argon temperature

quencies. The electron-ion frequency is estimated using established Coulomb collision theory, while the electron-neutral frequency is derived from momentum cross-sections sourced from the LXCAT database [33]. The collision frequencies are on the order of $\sim 10^8\,\text{s}^{-1}$. Given an electron thermal velocity of $\sim\!200$ km/s (for electrons at T = 2500 K), the electron mean free path is approximately 1–2 mm. This indicates that electrons should exhibit behavior characteristic of a rarefied regime, resembling particles rather than a continuum fluid, at least in the absence of a magnetic field.

In Fig. 8(b), the ratio of electron-ion to electron-neutral collision frequencies is plotted to underscore that the entire flow region operates in a fully developed Coulomb-dominated regime. The ratio values range from \sim 20 in the hot region to more than 250 in the freestream region. As a result, the unmagnetized electrical conductivity of the plasma corresponds to the Spitzer conductivity [34].

We now proceed to investigate parameters directly relevant for MHD interaction. The plasma electrical conductivity is of primary importance to estimate the magnitude of the electrical currents and electromagnetic volumic forces that could be generated in the flow in the presence of a magnetic field. Generally speaking, when a magnetic field is applied, the electrical conductivity of a plasma is a tensor and depends on the direction relative to the magnetic field direction. A generalized Ohm's law can be written as: [35]

$$\mathbf{j} = \sigma_{\parallel} \mathbf{E}_{\parallel} + \sigma_{\perp} (\mathbf{E}_{\perp} + \mathbf{v} \times \mathbf{B}) + \sigma_{\times} \mathbf{b} \times (\mathbf{E}_{\perp} + \mathbf{v} \times \mathbf{B})$$
 (1)

where **b** is the unit vector in the direction of **B**, **v** the flow velocity and **E** the total electric field (applied + induced). The orientation symbols (\parallel , \perp and \times are relative to the magnetic field) The three conductivities σ_{\parallel} , σ_{\perp} and σ_{\times} are respectively:

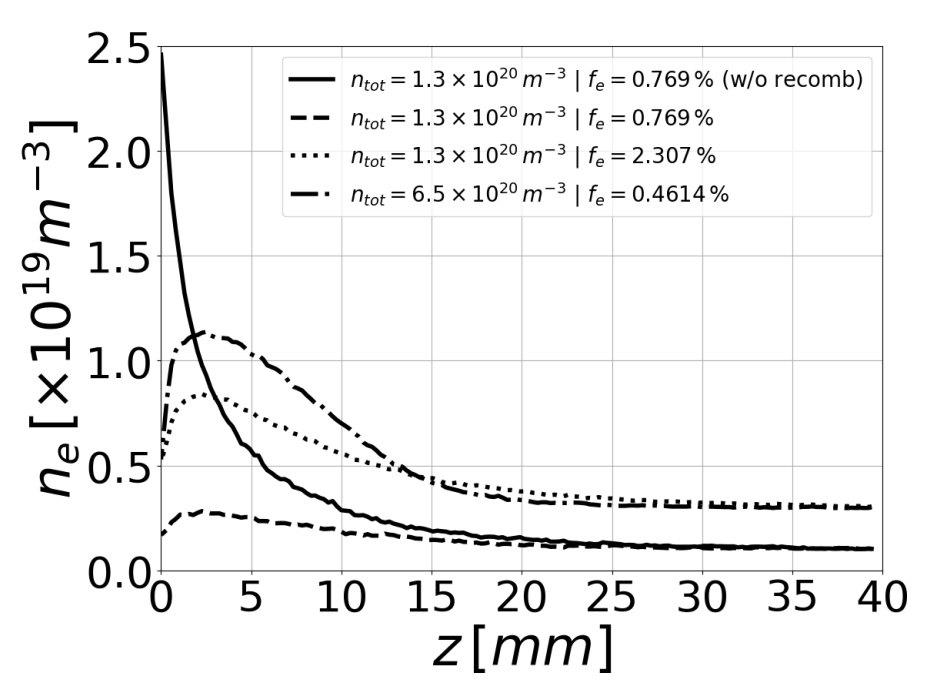


Fig 7. Lineouts of the electron density over the stagnation line for four different cases. z=0 corresponds to the model surface and the flow is oming from the right.

the Drude conductivity,

$$\sigma_{\parallel} = \frac{e^2 n_e}{m_e \nu_e} \tag{2}$$

the Pedersen conductivity,

$$\sigma_{\perp} = \sigma_{\parallel} \frac{1}{1 + \Omega_e^2} \tag{3}$$

and the Hall conductivity,

$$\sigma_{\times} = \sigma_{\parallel} \frac{\Omega_e}{1 + \Omega_e^2} \tag{4}$$

where ν_e is the total electron collision frequency and $\Omega_e = \omega_{ce}/\nu_e$ the electron Hall parameter with $\omega_{ce} = eB/m_e$ the electron cyclotron frequency. The Drude conductivity σ_{\parallel} corresponds to the plasma conductivity in the direction parallel to the local magnetic field, the Pedersen conductivity σ_{\perp} in the perpendicular ${\bf v} \times {\bf B}$ direction and the Hall conductivity σ_{\times} in the direction perpendicular to both ${\bf B}$ and ${\bf v} \times {\bf B}$. The electron Hall parameter quantifies the degree of electron magnetization. In the limit $\Omega_e \to \infty$, the conductivities in directions perpendicular to the magnetic field are suppressed, leaving only the parallel conductivity σ_{\parallel} .

As evident from the preceding discussion, accurate estimation of these parameters requires a precise definition of the magnetic field distribution surrounding the model. Fig. 9 illustrates the magnetic field magnitude (colormap) and streamlines (white lines) produced by a 15 mm \times 15 mm \times 24 mm magnet aligned with the main flow direction. This configuration corresponds to the one previously described in

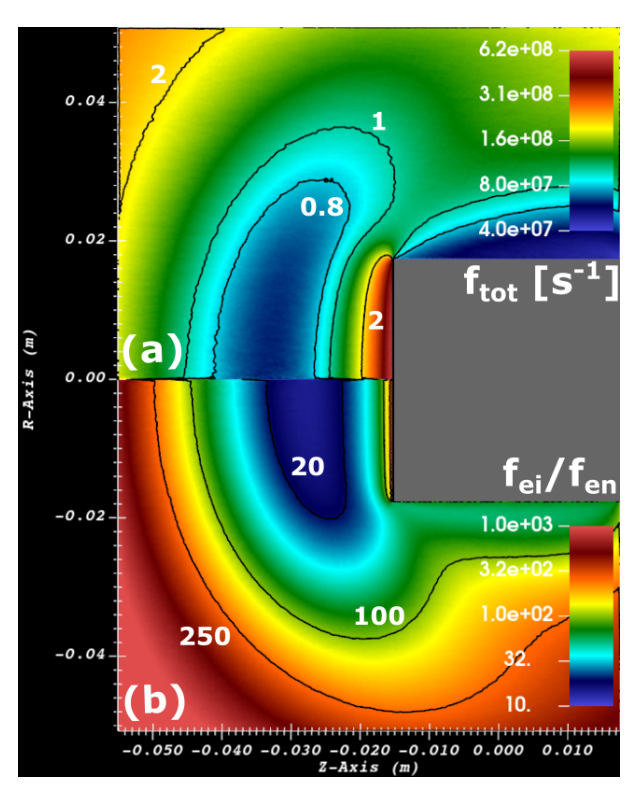


Fig 8. 2D (r-z) maps of (a) total electron collision frequency and (b) electron-ion to electron-neutral collision frequency

Fig. 3(b). The magnetic field distribution is modeled using the magpylib Python library [36]. Within the "plasma" domain, magnetic field strengths range from \sim 1 mT to \sim 0.1 T near the model surface.

By integrating the collision frequency maps from Figure 8 with the magnetic field distribution described above, we can now estimate the key quantities introduced earlier: the electron Hall parameter and the Drude, Pedersen, and Hall conductivities. These are illustrated in Figure 10(a), (b), (c), and (d), respectively. In Figure 10(a), the electron Hall parameter exhibits relatively high values, ranging from $\sim\!\!1$ near the inlet to $\sim\!\!50$ closer to the model in the shocked regions. In Figure 10(b), the standard Drude conductivity, which operates in the parallel direction, is on the order of $\sim\!\!400$ S/m in the freestream and approaches $\sim\!\!2000$ S/m in the hottest region (see Figure 6(d)). In the freestream regions, collisions remain significant and moderate the reduction in transverse conductivity values (σ_\perp and σ_\times). However, in the shocked regions, electrons are strongly magnetized, leading to substantial suppression of transverse conductivities—by a factor greater than 2000 for the Pedersen conductivity and approximately 50 for the Hall conductivity, as evident in Figure 10(c) and (d).

From these results, we can infer anticipated behaviors of the MHD interaction in this "aligned" configuration. In the absence of an applied electric field, the primary electromotive force inducing currents in the plasma is the $\mathbf{v} \times \mathbf{B}$ term. In most academic studies on MHD-induced effects in hypersonic flows, this current component is responsible for the observed phenomena, as electrons are typically not regarded as magnetized. Indeed, in the limit $\Omega_e \to 0$ with no electric field, the current simplifies to $\mathbf{j} = \sigma_{\parallel}(\mathbf{v} \times \mathbf{B})$. The resulting Lorentz force is then $\mathbf{j} \times \mathbf{B} = -\sigma_{\parallel} B^2 \mathbf{v}_{\perp}$ where \mathbf{v}_{\perp} is the flow velocity perpendicular to the magnetic field. It is evident that these forces consistently oppose the flow propagation direction, thereby decelerating the flow and allowing the generation of the so-called "MHD aero-braking" concept [37].

In the contrasting scenario where $\Omega_e \gg 1$ —as in our case—the dominant electrical current in the absence of an electric field is the Hall current: $\mathbf{j} = \sigma_{\times} \mathbf{b} \times (\mathbf{v} \times \mathbf{B}) = \sigma_{\times} B \mathbf{v}_{\perp}$. In the configuration illustrated

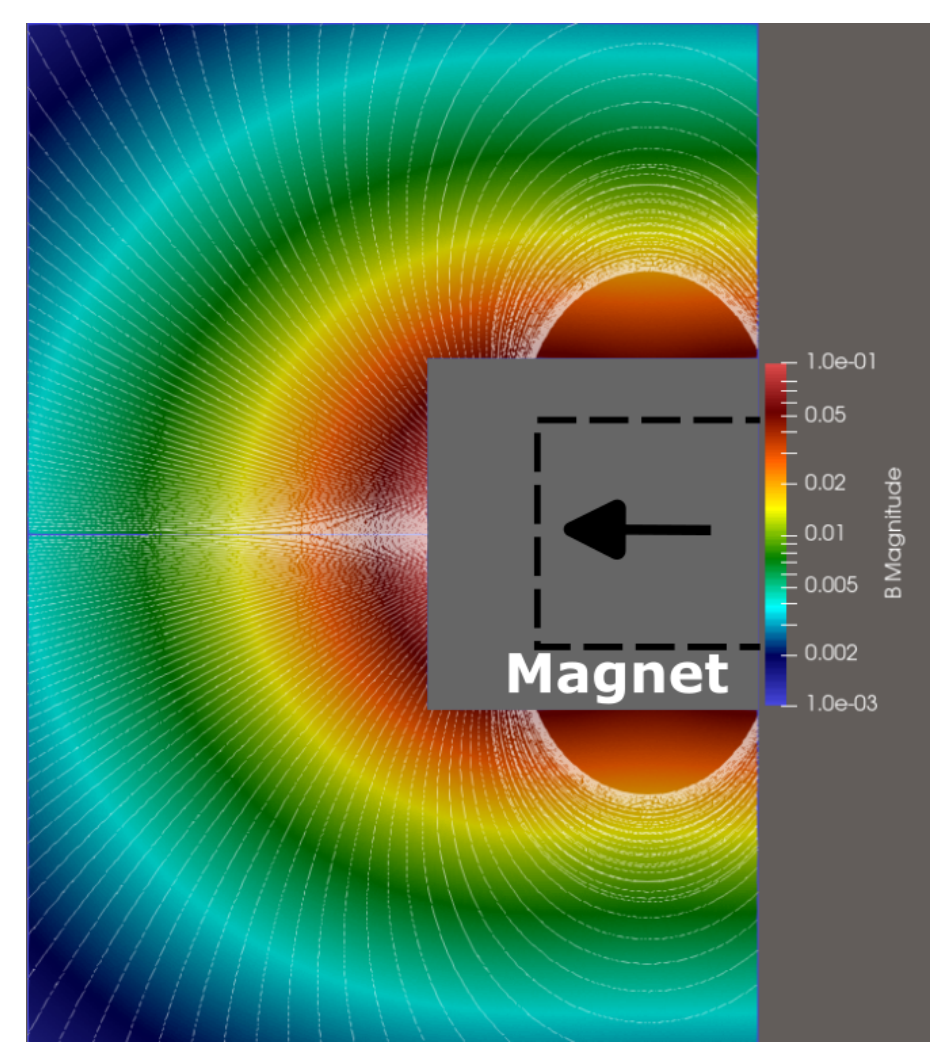


Fig 9. 2D map of the simulated magnetic field magnitude (colormap) and streamlines (white lines) produced by a 15 mm \times 15 mm \times 24 mm magnet embedded in the cylindrical support behind the model

in Figure 9, these currents circulate in the plane perpendicular to the magnetic field lines. The corresponding Lorentz forces are then $\mathbf{j} \times \mathbf{B} = \sigma_\times B^2 \mathbf{v}_\perp \times \mathbf{b}$, acting in the azimuthal direction perpendicular to the (r-z) plane. These forces induce a swirling motion in the flow and generate a corresponding roll moment on the model. Moreover, under our conditions, these forces are reduced by a factor of $\frac{\sigma_\parallel}{\sigma_\times} \approx \Omega_e \approx 50$ compared to those in the weakly magnetized case discussed previously.

This discussion elucidates why the Hall effect—prevalent in regimes with highly magnetized electrons—is frequently regarded as detrimental to MHD applications in aerospace. These conclusions must be approached with caution, however, as our analysis thus far has focused on a single magnetic configuration and, more critically, has omitted the influence of induced and self-induced electric fields. Such fields are nearly unavoidable in most configurations due to plasma inhomogeneities, model geometry, and material electrical properties. Therefore, resolving these induced electric fields is essential for accurately evaluating the significance of MHD effects in each configuration.

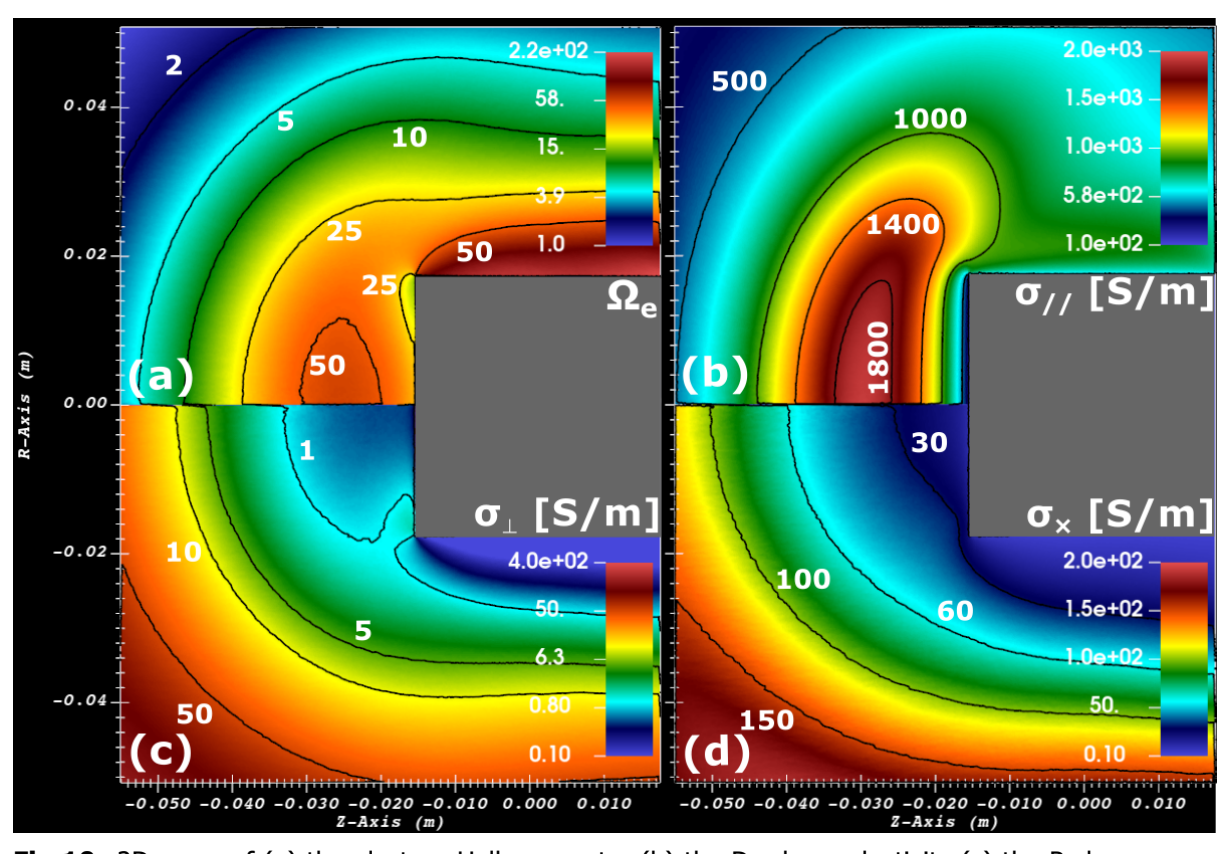


Fig 10. 2D maps of (a) the electron Hall parameter (b) the Drude conductivity (c) the Pedersen conductivity and (d) the Hall conductivity

5. A "test particle" numerical investigation of the magnetic field effect

As discussed in the previous section, electron trajectories in our experimental conditions are expected to be significantly influenced by the magnetic field. Given that the Hall parameter ranges from $\sim\!1$ to over 50, collisions are anticipated to play a non-negligible role, particularly far from the model or along magnetic field lines.

To explore these effects, we conducted "test-particle" numerical simulations of electron and ion trajectories across the experimental configurations, focusing on the setup illustrated in Figure 3(c). The leapfrog "Boris" scheme [38] was employed to integrate the 3D trajectories of charged particles over time. No electric field is considered in these simulations, and the magnetic field is generated using the magpylib Python library, consistent with prior modeling. Because of the dominant Coulomb regime, collisions are introduced using the Monte Carlo collisional scheme of [39]. For electron-ion collisions, ion population is considered "frozen" with a x-velocity of 3.5 km/s and a temperature of 2500 K.

Figure 11(a) illustrates the projections of electron trajectories in the (x-z) plane. Electrons are injected approximately 77 mm upstream from the magnet with an x-velocity matching the bulk plasma velocity (3.5 km/s). Shortly after injection, most electrons exhibit a pronounced deviation toward the magnet's poles. Due to the high degree of magnetization and the small Larmor radius, electrons are effectively constrained to follow the magnetic field lines.

Electrons injected near the z=0 plane display distinctly different trajectories, appearing not to reach the magnet surface. Examination of Figure 11(b), which depicts projections in the x-y plane, reveals that these particles—and indeed all electrons—are significantly deflected in the -y direction, corresponding to the $-\mathbf{v_i} \times \mathbf{B}$ direction. This deflection arises from the collisionally driven friction force on the electrons, which imparts the ion bulk velocity $\mathbf{v_i}$ to them. The resultant $-e(\mathbf{v_i} \times \mathbf{B})$ force shifts the particles in

this direction. Assuming that plasma self-emission is strongly correlated with electron density, these numerical findings align with the experimentally observed "arches" in Figure 3(c) and the asymmetry in Figure 3(d).

These qualitative preliminary results will be expanded and validated through more comprehensive simulations, particularly incorporating potential electric fields via the Particle-In-Cell method.

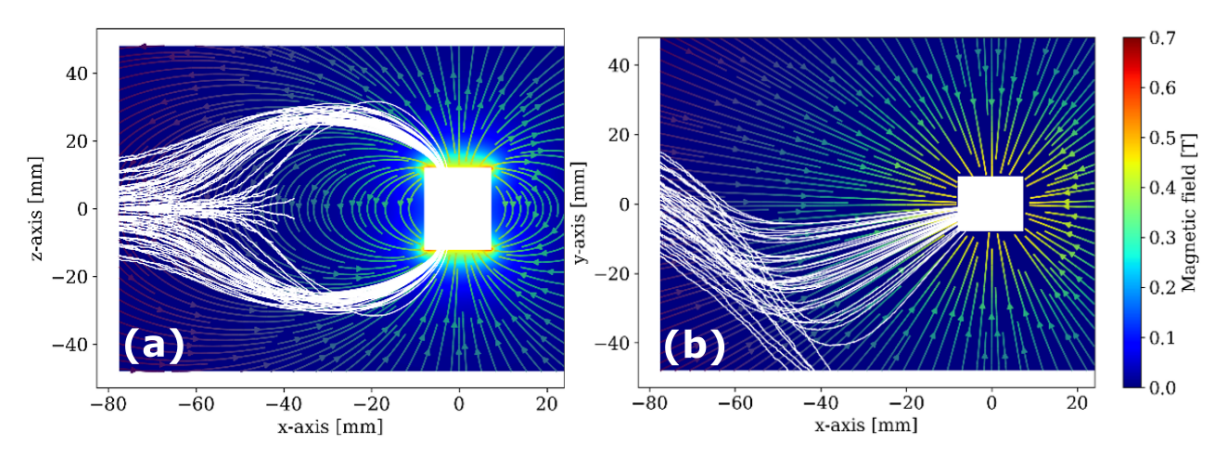


Fig 11. 2D projections of electron collisional and magnetized trajectories for configuration 3(c) (a) in the (x-z) plane (b) in the (x-y) plane. Colormap corresponds to the magnetic field magnitude. Magnet is shown as the white rectangle.

6. Conclusions

This study presents the initial MHD-relevant experimental results from the AMHYRA project. These preliminary findings confirm significant alterations in plasma-model interactions upon introducing a magnetic field, including: pronounced changes in plasma self-emission exhibiting strong dependence on field orientation, with the formation of "depleted" and "enriched" regions; an increase in shock standoff distance (up to ± 17 %); and modifications to the model surface state.

In-depth characterization of the MHD-relevant flow was conducted using DSMC simulations with the SPARTA code. This enabled inference of the full tensorial electrical conductivity of the plasma, incorporating the specified magnetic field distribution. Notably, the high Hall parameter regime leads to a dramatic reduction in $\mathbf{v} \times \mathbf{B}$ -induced currents. A simple "test-particle" approach was employed to model electron dynamics within the magnet's magnetic field, successfully reproducing several experimentally observed features.

Future work will expand flow characterization through spectroscopic diagnostics (for heavy particle temperature), Langmuir probes (for electron density n_e and temperature T_e), curling probes (for n_e) and aerodynamic efforts measurements. These enhancements will refine numerical simulations and provide a more accurate assessment of magnetic field effects. Additional plans include exploring alternative model geometries (e.g., blunt bodies) and conducting a deeper investigation into material influences, including degradation under magnetic fields. Numerical efforts will involve solving current conservation equations using the generalized tensorial Ohm's law, with DSMC fields as inputs. A more faithful, albeit computationally intensive, approach will utilize Particle-In-Cell simulations to model the various experimental configurations.

Aknowledgments

This research was supported by the Agence Nationale de la Recherche (ANR) and the Agence de l'Innovation de Défense (AID) under ASTRID project AMHYRA, grant number ANR-24-ASTR-0002. The authors would also like to thank Olivier de Bouët du Portal and Matthieu Mazallon for their help during the experimental campaign and the modelling work.

References

References

- [1] EL Resler Jr and W Re Sears. The prospects for magneto-aerodynamics. *Journal of the Aerospace Sciences*, 25(4):235–245, 1958.
- [2] Rudolph C Meyer. On reducing aerodynamic heat-transfer rates by magnetohydrodynamic techniques. *Journal of the Aerospace Sciences*, 25(9):561–566, 1958.
- [3] Richard W Ziemer and William B Bush. Magnetic field effects on bow shock stand-off distance. *Physical Review Letters*, 1(2):58, 1958.
- [4] Sung Min ($\square\square$) Jo, Marco Panesi, and Jae Gang ($\square\square$) Kim. Prediction of shock standoff distance with modified rotational relaxation time of air mixture. *Physics of Fluids*, 33(4):047102, 04 2021.
- [5] Richard J Rosa and James Kelley. Magnetohydrodynamic energy conversion, 1969.
- [6] EP Velikhov. Hall instability of current-carrying slightly-ionized plasmas. In *Proc. 1st Int. Symp. MPD Electr. Power Generation, Newcastle upon Tyne*, pages 135–162, 1962.
- [7] Donghoon Lee and Haecheon Choi. Magnetohydrodynamic turbulent flow in a channel at low magnetic reynolds number. *Journal of Fluid Mechanics*, 439:367–394, 2001.
- [8] Andrea Lani, Vatsalya Sharma, Vincent F Giangaspero, Stefaan Poedts, Alan Viladegut, Olivier Chazot, Jasmine Giacomelli, Johannes Oswald, Alexander Behnke, Adam S Pagan, et al. A magnetohydrodynamic enhanced entry system for space transportation: Meesst. *Journal of Space Safety Engineering*, 10(1):27–34, 2023.
- [9] Takayasu Fujino, Hiroyuki Sugita, Masahito Mizuno, Ikkoh Funaki, and Motoo Ishikawa. Influences of electrical conductivity of wall on magnetohydrodynamic control of aeroynamic heating. *Journal of Spacecraft and Rockets*, 43(1):63–70, 2006.
- [10] Zhifeng Zhou, Zhichao Zhang, Zhenxun Gao, Ke Xu, and Chun-Hian Lee. Numerical investigation on mechanisms of mhd heat flux mitigation in hypersonic flows. *Aerospace*, 9(10):548, 2022.
- [11] Minkwan Kim and Iain D Boyd. Effectiveness of a magnetohydrodynamics system for mars entry. Journal of Spacecraft and Rockets, 49(6):1141–1149, 2012.
- [12] Robert W Moses, F McNeil Cheatwood, Christopher O Johnston, Sergey O Macheret, Bernard Parent, Justin Little, RA Williams, Justin S Green, Matthew Austin, and Andrew Aldrin. New mhd lift concept for more efficient missions to mars and neptune. In *AIAA SCITECH 2022 Forum*, page 0934, 2022.
- [13] Min Kwan Kim. "Electromagnetic Manipulation of Plasma Layer for Re-Entry Blackout Mitigation". Michigan University, Ph.D. thesis, 2009.
- [14] David E Gildfind, Daniel Smith, Alexis Lefevre, Peter A Jacobs, and Timothy J McIntyre. Magnetohydrodynamic aerobraking shock stand-off measurements with flight representative electrodynamic boundary conditions. *AIAA Journal*, 60(1):41–55, 2022.
- [15] Jan Martinez Schramm and Klaus Hannemann. Study of mhd effects in the high-enthalpy shock tunnel göttingen (heg) using a 30 t-pulsed magnet system. In *International Symposium on Shock Waves*, pages 617–623. Springer, 2017.
- [16] Andrea Cristofolini, Carlo Borghi, Gabriele Neretti, Andrea Passaro, Antonio Schettino, Francesco Battista, Andrea Passaro, and Damiano Baccarella. Experimental activities on the mhd interaction in a hypersonic air flow around a blunt body. In *41st Plasmadynamics and Lasers Conference*, page 4490, 2010.

- [17] David E Gildfind, Daniel Smith, Steven W Lewis, Rory Kelly, Christopher M James, Han Wei, and Timothy McIntyre. Expansion tube magnetohydrodynamic experiments with argon test gas. In 2018 Flow Control Conference, page 3754, 2018.
- [18] Alexis Lefevre, David E Gildfind, Rowan J Gollan, Peter A Jacobs, and Christopher M James. Magnetohydrodynamic experiments of total heat flux mitigation for superorbital earth reentry. *AIAA Journal*, 60(9):5046–5059, 2022.
- [19] Romain Joussot, Viviana Lago, and Lago Viviana. Plasmas for high speed flow control. 12 2015.
- [20] Philippe Sagnier, Jean-Luc Verant, Dominique Devezeaux, Ajmal K Mohamed, and Alain Masson. Real gas flow characterization in the onera f4 high enthalpy wind tunnel. In *ICIASF'97 Record. International Congress on Instrumentation in Aerospace Simulation Facilities*, pages 378–388. IEEE, 1997.
- [21] Aymeric Bourlet, Julien Labaune, Fabien Tholin, Axel Vincent, François Pechereau, and Christophe O Laux. Numerical model of restrikes in dc gliding arc discharges. In *AIAA SCITECH 2022 Forum*, page 0831, 2022.
- [22] J. Porto, P. Q. Elias, and A. Ciardi. Anisotropic electron heating in an electron cyclotron resonance thruster with magnetic nozzle. *Physics of Plasmas*, 30(2):023506, 2023.
- [23] V Lago, R Joussot, and JD Parisse. Phedra: A high enthalpy wind tunnel for atmospheric entry simulations.
- [24] F. Boni, J. Jarrige, V. Désangles, and T. Minea. The curling probe: A numerical and experimental study. Application to the electron density measurements in an ECR plasma thruster. *Review of Scientific Instruments*, 92:033507, 2021.
- [25] F. Boni, B. Khiar, and V. Lago. A Novel Microwave Resonant Probe Diagnostic to Perform Real-Time and In-Situ Electron Density Measurements in Atmospheric Re-Entry Plasmas. In *4th International Conference on High-Speed Vehicle Science Technology*, pages HiSST–2025–342, Tours, 2025.
- [26] Konstantinos Baltzis. The femm package: A simple, fast, and accurate open source electromagnetic tool in science and engineering. *Journal of Engineering Science and Technology Review*, 1, 06 2008.
- [27] Theresa P Hennessey and JE Morral. Oxidation and nitridation of niobium in air above 1150° c. *Oxidation of metals*, 38(1):163–187, 1992.
- [28] Steve J Plimpton, SG Moore, A Borner, AK Stagg, TP Koehler, JR Torczynski, and MA Gallis. Direct simulation monte carlo on petaflop supercomputers and beyond. *Physics of Fluids*, 31(8), 2019.
- [29] Marcel Pfeiffer. An optimized collision-averaged variable soft sphere parameter set for air, carbon, and corresponding ionized species. *Physics of Fluids*, 34(11), 2022.
- [30] Krishnan Swaminathan-Gopalan and Kelly A Stephani. Recommended direct simulation monte carlo collision model parameters for modeling ionized air transport processes. *Physics of Fluids*, 28(2), 2016.
- [31] R Jacobs Gollan and Peter A Jacobs. About the formulation, verification and validation of the hypersonic flow solver eilmer. *International Journal for Numerical Methods in Fluids*, 73(1):19–57, 2013.
- [32] Shrey Trivedi, Jorge S Salinas, Myoungkyu Lee, Swapnil Desai, Michael A Gallis, John K Harvey, and Jacqueline Chen. Comparison of dsmc and multi-temperature simulations of thermal nonequilibrium in a supersonic kelvin-helmholtz shear layer. In *AIAA SCITECH 2024 Forum*, page 2722, 2024.
- [33] Emile Carbone, Wouter Graef, Gerjan Hagelaar, Daan Boer, Matthew M Hopkins, Jacob C Stephens, Benjamin T Yee, Sergey Pancheshnyi, Jan van Dijk, and Leanne Pitchford. Data needs for modeling

- low-temperature non-equilibrium plasmas: the lxcat project, history, perspectives and a tutorial. *Atoms*, 9(1):16, 2021.
- [34] Robert S Cohen, Lyman Spitzer Jr, and Paul McR Routly. The electrical conductivity of an ionized gas. *Physical Review*, 80(2):230, 1950.
- [35] Jean-Marcel Rax, Jean-Pierre Hulin, and Luc Petit. *Physique de la conversion d'énergie*. edp sciences, 2015.
- [36] Michael Ortner and Lucas Gabriel Coliado Bandeira. Magpylib: A free python package for magnetic field computation. *SoftwareX*, 11:100466, 2020.
- [37] Daniel R Smith, David E Gildfind, David J Mee, Christopher M James, and Barry V Allsop. Magneto-hydrodynamic drag force measurements in an expansion tunnel using a stress wave force balance. *Experiments in Fluids*, 61:1–15, 2020.
- [38] Charles K Birdsall and A Bruce Langdon. *Plasma physics via computer simulation*. CRC press, 2018.
- [39] F Pérez, L Gremillet, A Decoster, M Drouin, and E Lefebvre. Improved modeling of relativistic collisions and collisional ionization in particle-in-cell codes. *Physics of Plasmas*, 19(8), 2012.